research papers

High-spatial-resolution mapping of superhydrophobic cicada wing surface chemistry using infrared microspectroscopy and infrared imaging at two synchrotron beamlines

Mark J. Tobin,[a]* Ljiljana Puskar,[a] Jafar Hasan,[b] Hayden K. Webb,[b] Carol J. Hirschmugl,[c] Michael J. Nasse,[c,d] Gediminas Gervinskas,[e] Saulius Juodkazis,[e] Gregory S. Watson,[f] Jolanta A. Watson,[f] Russell J. Crawford[b] and Elena P. Ivanova[b]*

[a]Infrared Microspectroscopy Beamline, Australian Synchrotron, 800 Blackburn Road, Clayton, Victoria 3168, Australia, [b]Faculty of Life and Social Sciences, Swinburne University of Technology, PO Box 218, Hawthorn, Victoria 3122, Australia, [c]Department of Physics, University of Wisconsin-Milwaukee, 1900 E. Kenwood Road, Milwaukee, WI 53211, USA, [d]Karlsruhe Institute of Technology, Institute for Photon Science and Synchrotron Radiation, Hermann-von-Helmholtz-Platz 1, 76344 Eggenstein-Leopoldshafen, Germany, [e]Faculty of Engineering and Industrial Sciences (H34), Swinburne University of Technology, PO Box 218, Hawthorn, Victoria 3122, Australia, and [f]School of Marine and Tropical Biology, James Cook University, Townsville, Queensland 4811, Australia. E-mail: mark.tobin@synchrotron.org.au, eivanova@swin.edu.au

The wings of some insects, such as cicadae, have been reported to possess a number of interesting and unusual qualities such as superhydrophobicity, anisotropic wetting and antibacterial properties. Here, the chemical composition of the wings of the Clanger cicada (*Psaltoda claripennis*) were characterized using infrared (IR) microspectroscopy. In addition, the data generated from two separate synchrotron IR facilities, the Australian Synchrotron Infrared Microspectroscopy beamline (AS-IRM) and the Synchrotron Radiation Center (SRC), University of Wisconsin-Madison, IRENI beamline, were analysed and compared. Characteristic peaks in the IR spectra of the wings were assigned primarily to aliphatic hydrocarbon and amide functionalities, which were considered to be an indication of the presence of waxy and proteinaceous components, respectively, in good agreement with the literature. Chemical distribution maps showed that, while the protein component was homogeneously distributed, a significant degree of heterogeneity was observed in the distribution of the waxy component, which may contribute to the self-cleaning and aerodynamic properties of the cicada wing. When comparing the data generated from the two beamlines, it was determined that the SRC IRENI beamline was capable of producing higher-spatial-resolution distribution images in a shorter time than was achievable at the AS-IRM beamline, but that spectral noise levels per pixel were considerably lower on the AS-IRM beamline, resulting in more favourable data where the detection of weak absorbances is required. The data generated by the two complementary synchrotron IR methods on the chemical composition of cicada wings will be immensely useful in understanding their unusual properties with a view to reproducing their characteristics in, for example, industry applications.

Keywords: cicada wings; surface chemistry; FTIR; chemical mapping.

1. Introduction

The wings of insects such as the cicada, butterfly and dragonfly have been intensively studied at the micro- and nano-scale in relation to their superhydrophobic behaviour (Wagner *et al.*, 1996; Byun *et al.*, 2009). The superhydrophobicity of the surfaces of insect wings arises from a combination of the characteristic surface topography, in particular the nano-structure, and surface chemistry. Both characteristics contribute to the low surface energy of the material (Zhang *et al.*,

2009; Tanaka *et al.*, 2007; Watson *et al.*, 2008; Xie *et al.*, 2008). Cicada wing surfaces have been the subject of several studies that have demonstrated that both sides of the wings are homogeneously covered with hexagonal arrays of spherically capped conical nanoscale pillars (Watson *et al.*, 2008, 2010; Young *et al.*, 2009; Byun *et al.*, 2009), as shown in Figs. 1(*a*) and 1(*b*). The dimensions of the nanopillar arrays are known to vary according to species; for *Psaltoda claripennis* wings the nanopillars are 200 nm tall, 100 nm in diameter at the base, and 60 nm in diameter at the cap, and are spaced 170 nm apart from centre to centre (Sun *et al.*, 2009; Watson *et al.*, 2008; Ivanova *et al.*, 2012). The water contact angle on the wing surface of *P. claripennis* has been shown to vary between $147.4°$ and $171.5°$, with the average contact angle being $153°$ (Ivanova *et al.*, 2012), $150°$ being the threshold of super-hydrophobicity. Insect structures are typically composed of protein and the modified polysaccharide chitin. They also possess a layer of epicuticular waxes which are expected to substantially contribute to their high contact angles (Gorb *et al.*, 2000; Kreuz *et al.*, 2001; Lockey, 1960).

Infrared (IR) microspectroscopy allows the chemical composition of materials to be investigated based on the IR absorbance spectrum obtained from a defined area within the sample. Coupling of a Fourier transform infrared (FTIR) spectrometer and microscope to a synchrotron beamline provides a highly focused IR 'probe' beam with a typical dimension of approximately 8 μm in diameter, and an intensity within the focus which is up to $100\times$ brighter than is possible with conventional broadband IR sources. Mapping of the sample through this focused IR beam enables spatially resolved chemical maps to be built up pixel by pixel with a spatial resolution at, or very close to, the diffraction limit (depending on aperture setting and wavelength) and, most importantly, with very low spectral noise. These characteristics make synchrotron IR microspectroscopy ideal for probing the composition of samples which are only a few micrometres to several tens of micrometres in size. This point mapping approach is employed at the IR Microspectroscopy beamline at the Australian Synchrotron (Heraud *et al.*, 2010). More recently an alternative approach has been developed whereby a very large horizontal opening angle of synchrotron-generated IR light is coupled to an FTIR microscope equipped with a focal plane array (FPA) IR imaging detector. This allows IR spectral images, which have higher spatial resolution and are diffraction-limited at all mid-IR wavelengths, to be collected over much larger spatial dimensions in a much shorter time than is possible using either the mapping method employed at most synchrotron beamlines, or when using laboratory-based FPA FTIR microscopes. The IRENI beamline IR microscope at the Synchrotron Radiation Center (SRC), University of Wisconsin-Madison, is equipped with a 128×128 element IR FPA detector (in this paper we used only 64×64 pixels), and is set up such that the pixel resolution gives a sampling interval of 0.54 μm projected sample length per detector pixel (Nasse *et al.*, 2011). At a wavelength of 6 μm (which corresponds approximately to the amide I absorbance of protein at 1650 cm^{-1}), when using the highest numerical aperture (NA)

IR objective commercially available (NA = 0.65), the measured diffraction-limited spatial resolution, for a Schwarzschild optic, is approximately 3 μm, and the measured resolution at 2800 cm^{-1} (3.5 μm wavelength) is approximately 1.9 μm. Note that these values are somewhat better than the calculated ones (5.6 and 3.3 μm, respectively) from the conventional Rayleigh formula, $0.61 \times$ wavelength/NA, partially due to the Schwarzschild geometry. The small pixel size represents a spatial oversampling, giving the optimum conditions for resolving sample features of these dimensions (Stelzer, 1998). There is, however, a trade-off in signal-to-noise per pixel resulting both from the simultaneous illumination of 4096 individual detector elements, and from the higher noise level inherent to such FPA detector elements in comparison with single-element mercury cadmium telluride (MCT) IR detectors typically used for single point IR mapping measurements. A further limitation is that the sensitivity of FPA detectors, compared with MCT single-element detectors, drops greatly below 850 cm^{-1}, whereas narrowband MCT single-element detectors are sensitive to around 750 cm^{-1}, and wideband detectors to 500 cm^{-1}.

In this paper we provide further insight into the chemical composition and spatial distribution of the major components on the *Psaltoda claripennis* wing surfaces. Initial investigation of the *P. claripennis* wings was performed using the Infrared Microspectroscopy beamline at the Australian Synchrotron (AS-IRM). Further investigation was then performed at high spatial resolution over larger areas of the insect wings, using the recently developed synchrotron IR imaging beamline IRENI, located at the SRC, Stoughton, WI, USA. Using the IR beamlines situated at two synchrotrons, the aim of the study was firstly to characterize the chemical distribution of various components of the cicada wings, and secondly to provide a comparison of the data acquisition capabilities of the two IR beamlines.

2. Materials and methods

2.1. Insect wing sample preparation

Cicada (*Psaltoda claripennis*) samples were collected from the Brisbane parkland areas followed by removal of the wings using scalpel or scissors. The wings (approximate thickness 5 μm) were then cut into squares approximately 0.5 cm in width and rinsed with MilliQ H$_2$O (resistivity of 18.2 MΩ cm^{-1}) before being used for experimental analysis (Ivanova *et al.*, 2012). For IR microscopy, wing samples were mounted into a metal support frame which fitted onto the motorized stage of the IR microscopes at both the AS-IRM and IRENI beamlines.

2.2. Optical profilometry

The surface topography was initially analysed using the Bruker AXS Contour GT three-dimensional optical profiling system in white-light vertical-scanning interferometry mode using objectives of different magnifications varying from $10\times$ to $230\times$. Three samples of each surface type were briefly

scanned to evaluate the overall homogeneity of the surface and then the topographical profiles were studied at five different locations.

2.3. Scanning electron microscopy

High-resolution scanning electron microscopy (SEM) images of cicada wings were taken using a field-emission SEM (Raith150-TWO, Germany) at 5 kV under different magnifications. Prior to viewing samples under the microscope, insect wings were coated with thin gold films using a Dynavac CS300 according to the previously developed procedure reported by Mitik-Dineva *et al.* (2009).

2.4. Infrared microspectroscopy at the Australian Synchrotron

The spatially resolved distribution of chemical functional groups present across selected areas of the cicada wing was mapped and characterized by FTIR microspectroscopy in transmission mode over several areas of approximately 50 μm × 50 μm. The regions were mapped at the Australian Synchrotron IRM beamline (Clayton, Victoria, Australia) which was equipped with a Bruker Hyperion 2000 FTIR microscope (Bruker Optic GmbH, Ettlingen, Germany). The microscope was operated with a 36× (NA = 0.5) reflecting objective and condenser and a narrowband MCT detector, coupled to a Bruker V80v FTIR spectrometer. The microscope and spectrometer were controlled though *OPUS* (version 6.5) software, which was also used for data analysis. IR map data sets were collected by rastering the sample stage in a programmed pattern, with IR absorbance spectra collected at set spatial intervals of 2 μm using a single aperture in a focal plane between the sample and detector to define a 5 μm × 5 μm measurement region per position on the sample. A background spectrum was collected through air at repeated intervals during each map. Spectra were collected at 8 cm^{-1} spectral resolution with eight scans co-added for each measurement position, with the time required for map collection being approximately 4 s per pixel. This time includes a large instrumental time overhead arising from the *OPUS* software's requirement to move the sample stage position, check aperture dimensions and initiate the new scan at each position within the map. Actual data acquisition accounted for only 0.5 s of the 4 s taken to progress between pixel positions across the sample. Functional group maps were generated from the data by integration of the area under each absorption curve comprising an IR map data set, specifying the start and end wavenumber from which both the integration and a straight baseline were taken. Amide II integration was calculated from 1588 to 1483 cm^{-1}, and ν_{as} CH$_2$ integration was taken from 2931 to 2913 cm^{-1}. Each map had a spatial smoothing function applied using the Bruker *OPUS* 'Contour Colours' function.

2.5. IR microspectroscopy at the SRC

IR spectral images of a cicada wing were collected at the IRENI IR imaging beamline at the SRC (Stoughton, WI, USA). The IRENI beamline extracts 320 mrad (h) by 27 mrad (v) of light from a single bending magnet of the ALADDIN storage ring, splitting this into 12 separately collimated parallel beams which are arranged in a 3 × 4 array prior to entering a Bruker V70 FTIR spectrometer and Hyperion 3000 microscope. The result of this optical configuration is a 3 × 4 array of brightly illuminated areas on the sample, and hence on the FPA detector. The microscope was operated in transmission mode and was equipped with a 20× condenser and 74× objective (NA = 0.65) giving a detector field of view of 34.5 μm × 34.5 μm in the sample plane, and a projected sample length on each detector pixel of 0.54 μm. Slight defocusing of the microscope condenser enabled the field of view, and hence a selected 64 × 64 element region of the FPA detector, to be evenly illuminated by the 12 synchrotron beams. This resulted in a sample illumination which typically varied in intensity from 4000 counts to 6500 counts per pixel across the detector frame. Multi-image maps were collected with a repeated background image collected between each sample image of the map, co-adding 64 scans at a spectral resolution of 6 cm^{-1}, with acquisition of each sample and background image taking a combined time of 126 s. Data acquisition and analysis were undertaken using Bruker *OPUS* software (version 6.5), and functional group maps were generated from the IRENI beamline data sets using the same integration parameters as were applied to the AS-IRM beamline data sets.

3. Results and discussion

3.1. Micro- and nano-scale surface topography of cicada wings

Fig. 1(*a*) shows a photograph of the cicada in this study perched on native flora. Optical profiling of a cicada wing showed a mainly smooth surface between the wing bars (Fig. 1*b*), with some submicrometer roughness observed at higher magnification (Fig. 1*b*, inset). SEM confirmed the presence of nanoscale surface pillars in a hexagonal array (Fig. 1*c*).

3.2. Determination of chemical compounds present in cicada wings by FTIR spectroscopy

FTIR transmission spectra acquired at the AS-IRM beamline showed a series of absorbance bands which are consistent with the expected overall composition of cicada wings (Fig. 1*d*). The major peaks include amide I (predominantly C=O stretching coupled to N—H bending, 1610–1695 cm^{-1}) and amide II (C—N stretch coupled to N—H bending, 1480–1575 cm^{-1}) of amide functional groups, both of which can be attributed to chitin and proteins (Sajomsang & Gonil, 2010; Brugnerotto *et al.*, 2001; Ganim *et al.*, 2008; Caruso *et al.*, 1998). The spectral region between 2840 and 3000 cm^{-1} contains the symmetric (ν_s) and antisymmetric (ν_{as}) C—H stretching absorbances of CH$_2$ and CH$_3$ functional groups. The presence of these C—H stretching bands together with the relative prevalence of the methylene bands compared with the methyl
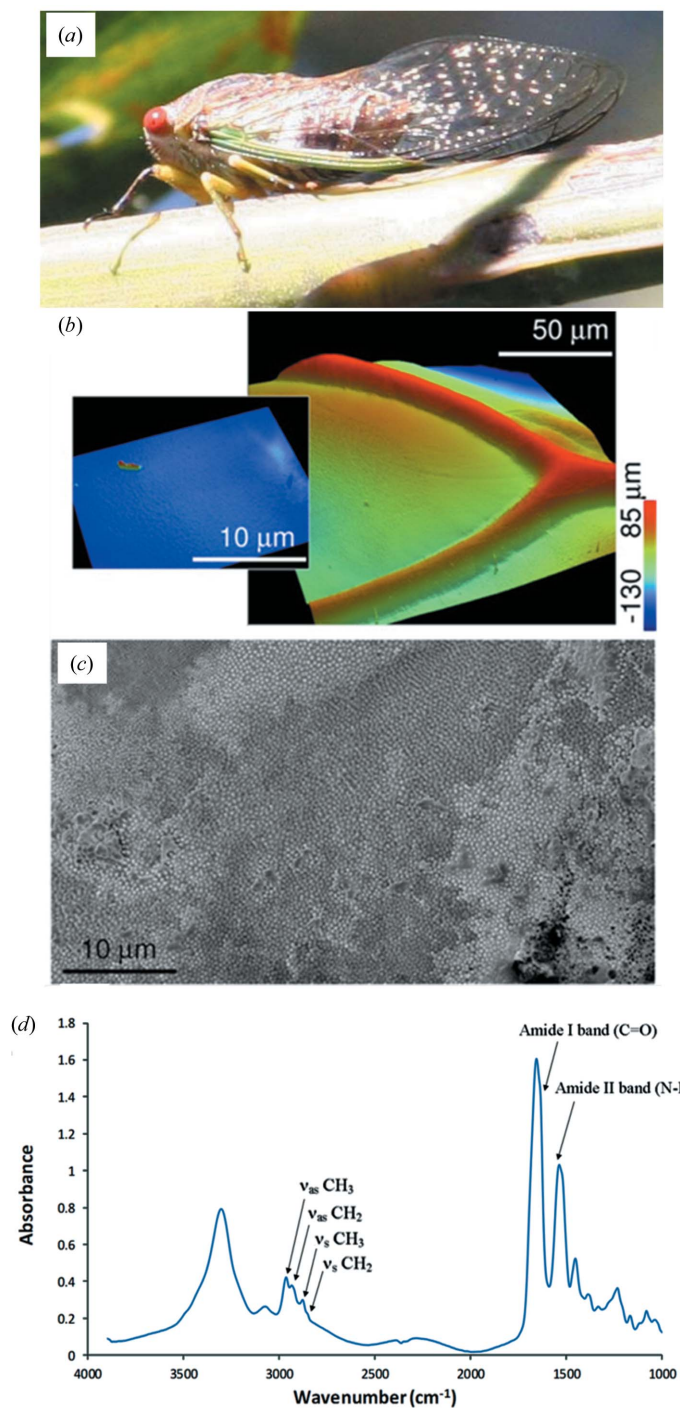
Figure 1
(a) Cicada *Psaltoda claripennis* perched on native flora. (b) Optical profiling of a cicada wing at different magnifications. The inset on the left shows a close-up view of a flat region of the wing membrane while the image on the right shows a lower magnification view, which includes a wing vein. (c) SEM image. (d) Typical FTIR spectrum of a cicada wing membrane showing molecular absorption bands of various peaks of interest.

bands is indicative of long-chain hydrocarbons, which can most likely be attributed to the cuticular waxes that are generally present on insect surfaces (Zeier & Schreiber, 1999; Merk *et al.*, 1997; Blom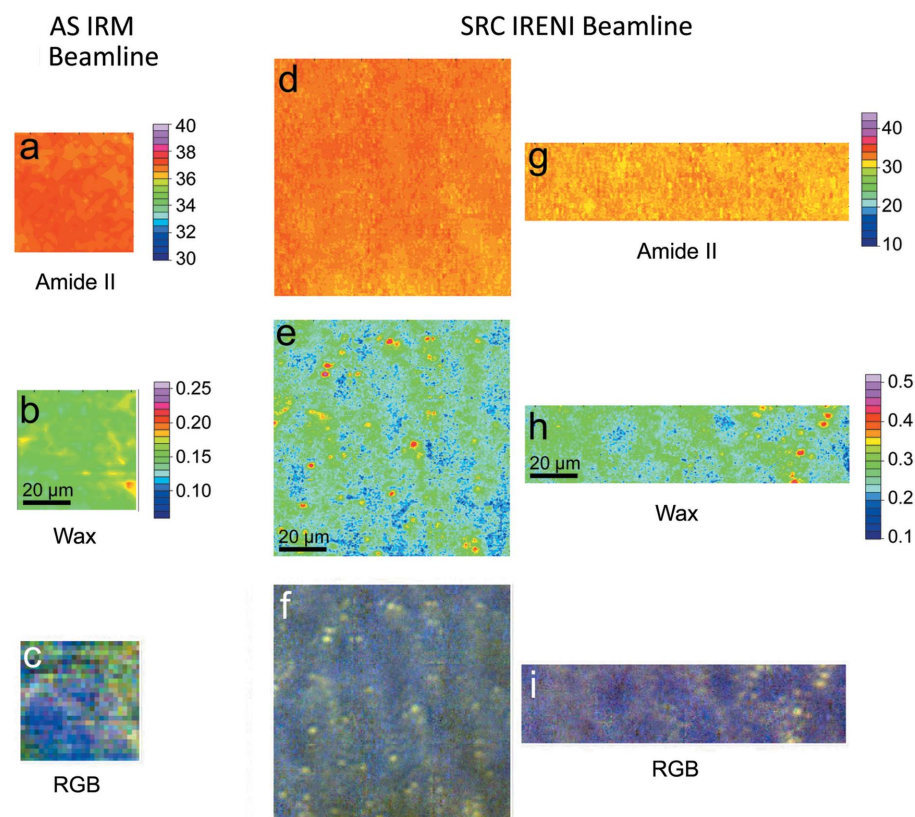quist & Bagnères, 2010). These initial findings confirm that the wing membranes are mainly composed of chitin, proteins and waxes.

3.3. Functional group mapping of cicada wings

Analysis of the IR absorbance maps from the Australian Synchrotron IRM beamline showed some spatial heterogeneity of the total integrated area of the CH_2 and CH_3 stretching region. Closer inspection of absorbance peaks in spectra with low and high total C—H stretching absorbance revealed that variation in ν_s CH_2 and ν_{as} CH_2 peaks relative to the ν_s CH_3 and ν_{as} CH_3 peaks accounted for most of the variation in total C—H absorbance observed across the wing membrane. Furthermore, in locations where the ν_{as} CH_2 peak showed increased intensity, the peak was also shifted to lower wavenumber, allowing more precise integration of this peak area for the generation of CH_2 distribution maps. The IR absorbance distribution maps shown in Fig. 2 were obtained by integration of amide II and ν_{as} CH_2 peaks using the spectral limits given in §2. The amide II peak was used in preference to the amide I band as the latter showed evidence of saturation in some locations. Fig. 2(a) shows an amide II integration map for a 50 µm $\times$ 50 µm (25 $\times$ 25 pixels) area of cicada wing mapped using the AS-IRM beamline. The map reveals a relatively homogeneous distribution of protein/chitin components across the wing, even with the colour scale compressed to cover a range from 30 to 40 integrated absorbance units. In contrast, the integration map for the ν_{as} CH_2 band shows clear evidence of heterogeneity in the distribution of long-chain hydrocarbon components (Fig. 2b). A corresponding RGB (red, green and blue) pixel image generated from the same data set is shown in Fig. 2(c), which demonstrates the combined distribution of amide II (blue) and ν_{as} CH_2 (red + green) over the same area.

High-spatial-resolution chemical distribution maps generated from data sets obtained at the IRENI beamline present a similar picture. Over an area of approximately 104 µm $\times$ 104 µm, the amide II distribution is largely homogeneous, while the ν_{as} CH_2 is much more heterogeneous [Figs. 2(d) and 2(e)]. Differences in the scale-bar range required to visualize the amide II data, compared with the data from the AS-IRM beamline, probably arise from differences in the wing thickness between the measurements. Different scale-bar ranges for the CH_2 wax maps were used to allow the well resolved highly absorbing spots of wax in the IRENI data to be presented, while still showing the smaller variations in wax distribution that were detected at the AS-IRM beamline. The corresponding RGB composite pixel image appears similar to that of the AS-IRM data set, albeit at higher lateral resolution (Fig. 2f). A second set of maps was generated from IRENI data using rectangular dimensions (138 µm $\times$ 35 µm) in order to examine the chemical distributions over larger lateral distances. The resulting maps demonstrate that very similar variations are observable in the protein/chitin and wax components of the wings in this second area of wing membrane [Figs. 2(g)–2(i)].

The heterogeneity of the ν_{as} CH_2, *i.e.* the wax component, is characterized by multiple localized high-intensity spots, irre-

Mark J. Tobin *et al.* · Mapping of superhydrophobic cicada wing surface chemistry

Figure 2
Chemical intensity maps of amide II and CH_2 absorbance peaks obtained by integration of the respective peaks (amide II: 1588–1483 cm^{-1}; ν_{as} CH_2: 2931–2913 cm^{-1}). (a)–(c) represent the images obtained from the IR scans performed at the IR Microspectroscopy beamline at the Australian Synchrotron while (d)–(i) are respective images obtained from the IRENI beamline, SRC, University of Wisconsin-Madison, USA. The intensity of the integrated area of the amide II band [(a), (d) and (g)] and CH_2 antisymmetric stretching [(b), (e) and (h)] are shown in consistent colour scale between beamlines, but with the value range compressed for the amide II maps, to enhance the low level of variation, in particular in image (a). RGB (red, green, blue) composite images [(c), (f) and (i)] show the blended presence of amide II and CH_2 antisymmetric stretching, with R + G representing long-chain hydrocarbon (wax) and B showing amide II (protein). Map dimensions are: 50 μm × 50 μm [(a)–(c)], 104 μm × 104 μm [(d)–(f)], 138 μm × 35 μm [(g)–(i)].

gularly spaced across the wing. The IRENI beamline data show this particularly clearly, in addition to a secondary network-like variation over a length scale of a few tens of micrometres [Figs. 2(f) and 2(i)], a pattern which had not been clearly resolved using the AS-IRM beamline. The IRENI beamline is clearly able to resolve the wax spots with an apparent lateral resolution of approximately 3.5 μm, based on the diameter of the observed spots.

3.4. Composition and location of the heterogeneous wax component

To further investigate the nature of the observed heterogeneity in the wax distribution, a spectral subtraction was performed using spectra extracted from points of both high and low intensity in ν_{as} CH_2 integration maps from the IRENI beamline (Fig. 3). After subtraction, the only significant peaks that remained in the C—H stretching region of the spectrum were those corresponding to the ν_s CH_2 and ν_{as} CH_2 vibrations (Fig. 3b), consistent with a long-chain hydrocarbon similar to

paraffin. Spectra collected from locations across cicada wings that had been treated for 1 h with chloroform, in order to remove soluble components from the wing surface, did not show the strong shifted ν_s CH_2 and ν_{as} CH_2 peaks that were observed in spectra from points within the untreated wings (data not shown). This confirms that the ν_{as} CH_2 absorbance maps presented here from both IR beamlines illustrate the heterogeneous distribution of a waxy material that is located on the surface of the cicada wing.

To enhance visualization of the wax distribution, a further map was produced using the same data set that is shown in Figs. 2(d)–2(f), but in which the ratio of the integrated areas of the ν_{as} CH_2 and ν_{as} CH_3 bands was calculated. The ratio map is shown as a three-dimensional plot in Fig. 4. Calculation of this ratio in part reduces the contribution to the 'wax' image that may derive from the slight variation in ν_{as} CH_2 resulting from absorbance by the wing membrane. The visible image of the same wing area, which is shown underneath the three-dimensional wax plot in Fig. 4, reveals some weakly contrasting features (arrowed), but these do not correspond to the locations of the observed wax inclusions.

Long-chain hydrocarbons in insects are generally known for decreasing the wettability of the wings (Blomquist & Bagnères, 2010). Our data show that in the case of the cicada wing the hydrocarbon coating is distributed in a patterned array of spots, of a few micrometres in size, distributed in a network with a length scale of a few tens of micrometres. The occurrence of this heterogeneous wax distribution might suggest a variation in the superhydrophobic properties of the wing over a scale of just a few micrometres. This is in good agreement with our previous findings where the contact angle values ranged from 147 to 171° over similar distances (Ivanova et al., 2012). The regions of high and low wax distribution on cicada wings may assist the insect in developing a range of functionalities which may include self-cleaning, antifouling, antibacterial activities, aerodynamic efficiency and combating predation (Grimaldi & Engel, 2005; Wagner et al., 1996; Ivanova et al., 2012).

The understanding gained about the structure and composition of cicada wings at the micrometre scale could prove useful in designing and reproducing superhydrophobic surfaces with variable wax distributions in order to imitate different functionalities as present in the native state of the wings (Ivanova et al., 2012). Different applications of super-
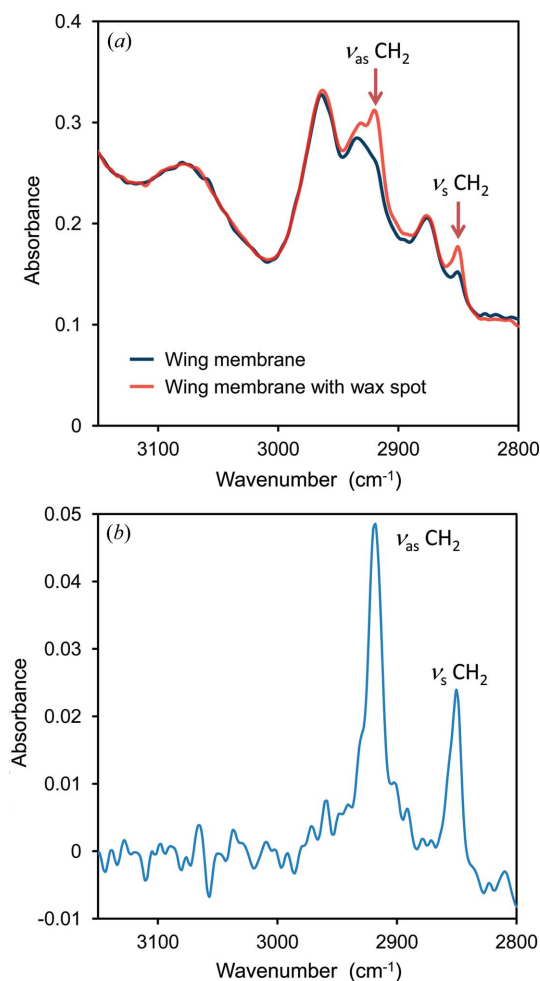
Figure 3 appears on the left with two panels (a) and (b).

Figure 4
The ratio of intensity maps of CH_2 and CH_3 antisymmetric stretching is shown as a three-dimensional overlay above a visible-light image of the wing membrane. Some weakly contrasting features observable in the visible image are arrowed. The area shown is approximately 104 µm × 104 µm.

Figure 3
Single-pixel spectral analysis of data from the IRENI beamline, obtained from regions showing higher wax peak intensity (*a*, red) and low wax peak intensity (*a*, blue). Spectrum subtraction of the low wax spectrum from the high wax spectrum (*b*).

hydrophobic surfaces include textile engineering, medical implants, antifouling coatings, microfluidics and aerodynamics (Yao *et al.*, 2011; Zimmermann *et al.*, 2008; Ramananarivo *et al.*, 2011; Banerjee *et al.*, 2011; Webb *et al.*, 2011; Salta *et al.*, 2010).

3.5. Comparison of data from the AS-IRM and IRENI synchrotron beamlines

Comparison of the spatial resolution of the SRC IRENI beamline with the AS-IRM beamline indicates that the IRENI beamline is capable of clearly resolving features over a large area at a very high resolution level which is at the theoretical wide-field diffraction limit. This is enabled by the optical configuration of the 74× objective combined with the FPA detector, resulting in a significant spatial oversampling across the sample plane, with a projected sample pixel size at the detector of 0.54 µm × 0.54 µm. In contrast, the AS-IRM beamline is limited in the area it can cover within a reasonable time by the need to acquire data point-by-point, and the data presented here were collected with an aperture setting of 5 µm
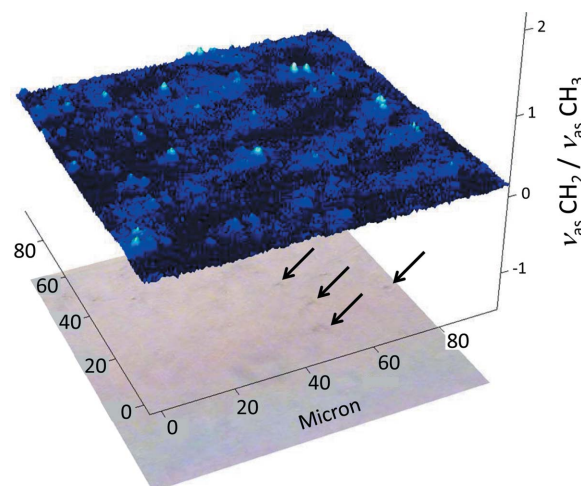
and a spatial step size of 2 µm. The significant spatial over-sampling achieved by the IRENI beamline also makes possible the use of point-spread-function deconvolution of image data to further enhance spatial resolution (Mattson *et al.*, 2012), a step which was not applied to the data presented here.

An assessment of spectral noise was made for data collected at both the AS-IRM beamline and at the SRC IRENI beamline. Spectra extracted from the IRENI data sets presented here were compared with additional spectra collected at the AS-IRM beamline, but recorded at 6 cm^{-1} spectral resolution and with an aperture of 4 µm × 4 µm so as to enable a more direct comparison to be made between data sets. RMS noise was measured using Bruker *OPUS* 6.5 software in a spectral region from 2450 to 2550 cm^{-1} for individual spectra, after conversion from absorbance to percentage transmission, and values are reported as a percentage noise. Three spectra selected from the AS-IRM beamline data gave an average noise value per pixel of 0.073%, for eight co-added scans at 6 cm^{-1} resolution. Three spectra from the SRC IRENI beamline gave an average noise value per pixel of 0.330% for spectra of 64 scans at 6 cm^{-1} resolution, and pixel binning of these data showed that a binning level of 8 × 8 pixels, representing the latter results as if they were collected with 4.32 µm × 4.32 µm sample projected pixels, was required to achieve an average noise level from three selected locations of 0.081%. Thus, the noise for the two recorded results, for similar spatial measurement areas of approximately 4 µm × 4 µm, is broadly equivalent. Nevertheless, only eight scans were co-added for the AS-IRM data, in contrast to 64 scans for IRENI, the latter being required to overcome the noisier characteristics of the FPA detector. In further comparison, collection of 64 scans at the AS-IRM beamline reduced the RMS noise level at 4 µm × 4 µm aperture and 6 cm^{-1} resolution to 0.022%.

A comparison can also be made of the time required to collect a data set of equivalent signal to noise, over a similar spatial area (but with very different spatial resolution). Each single FPA image, collecting 64 scans at 6 cm^{-1} spectral resolution, took 126 s to acquire (63 s each for background and sample images). A map of 8 × 8 pixels (equivalent in data content to an 8 × 8 pixel-binned 64 × 64 FPA image) recorded with 8 scans at 8 cm^{-1} spectral resolution by point mapping would take approximately 288 s to acquire, at 4 s per pixel with one background spectrum recorded per sample row. To achieve the spatial oversampling at 0.54 μm per pixel achieved at IRENI, but using the AS-IRM beamline mapping as described in this paper, one would require approximately 130 times longer data collection to cover an equivalent sample area than was required at IRENI. The spectra from each mapped pixel would, however, have much lower noise than the data from IRENI. This illustrates the advantage gained by FPA instruments through parallel acquisition from multiple detector elements, though efforts to reduce the dead-time between measurements in a point-mapping instrument could in future reduce the gap in acquisition times.

These results indicate that the capabilities of the two facilities, and the two approaches to synchrotron IR microspectroscopy, are complementary. Synchrotron FPA imaging is capable of rapidly analysing large areas at high spatial resolution, while point mapping with a single focused beam is able to probe small samples features with the very high spectral signal to noise necessary to observe more subtle spectral differences and weakly absorbing samples.

4. Summary and conclusions

The chemical composition of the wings of *Psaltoda claripennis* cicadae was analysed using the IR microspectroscopy facilities at two synchrotrons: the Australian Synchrotron and the Synchrotron Radiation Center. The wings were found to be composed of materials similar to those typically associated with insects, in the form of protein, chitin and waxes. Spatial mapping of chemical groups showed that the protein and chitin content was consistent throughout the wing; however, the distribution of waxes varied, with a punctuate distribution on a length scale of a few micrometres. The heterogeneous wax distribution on cicada wing surfaces may play a functional role in some of the unusual qualities of the wing, in particular the self-cleaning and directed wettability properties. The data presented here will aid in the fundamental understanding and ultimately the reproduction of the interesting properties of insect wings for industrial applications. Furthermore, the study of similar samples at two technically different IR beamlines has allowed the comparison of IR mapping using a focused synchrotron beam with the more recent development of synchrotron IR imaging using a focal plane array detector. Our data demonstrate that for synchrotron IR beamlines the highest spatial resolution can be achieved rapidly, and over large areas, through the combination of a multi-element FPA detector with high-magnification microscope optics and a synchrotron beam, whereas the lowest noise spectra are to be obtained from microscopic samples with a highly focused beam and single-element detector.

References

Banerjee, I., Pangule, R. C. & Kane, R. S. (2011). *Adv. Mater.* **23**, 690–718.

Blomquist, G. J. & Bagnères, A.-G. (2010). *Insect Hydrocarbons Biology, Biochemistry and Chemical Ecology.* Cambridge University Press.

Brugnerotto, J., Lizardi, J., Goycoolea, F., Argüelles-Monal, W., Desbrières, J. & Rinaudo, M. (2001). *Polymer*, **42**, 3569–3580.

Byun, D., Hong, J., Saputra, Ko, J. H., Lee, Y. J., Park, H. C., Byun, B. & Lukes, J. R. (2009). *J. Bionic Eng.* **6**, 63–70.

Caruso, F., Furlong, D. N., Ariga, K., Ichinose, I. & Kunitake, T. (1998). *Langmuir*, **14**, 4559–4565.

Ganim, Z., Chung, H. S., Smith, A. W., Deflores, L. P., Jones, K. C. & Tokmakoff, A. (2008). *Acc. Chem. Res.* **41**, 432–441.

Gorb, S. N., Kesel, A. & Berger, J. (2000). *Arthropod Struct. Dev.* **29**, 129–135.

Grimaldi, D. A. & Engel, M. S. (2005). *Evolution of the Insects.* Cambridge University Press.

Heraud, P, Caine, S., Campanale, N., Karnezis, T., McNaughton, D., Wood, B. R., Tobin, M. J. & Bernard, C. C. A. (2010). *NeuroImage* **49**, 1180–1189.

Ivanova, E. P., Hasan, J., Webb, H. K., Truong, V. K., Watson, G. S., Watson, J. A., Baulin, V. A., Pogodin, S., Wang, J. Y., Tobin, M. J., Löbbe, C. & Crawford, R. J. (2012). *Small*, **8**, 2489–2494.

Kreuz, P., Arnold, W. & Kesel, A. B. (2001). *Ann. Biomed. Eng.* **29**, 1054–1058.

Lockey, K. H. (1960). *J. Exp. Biol.* **37**, 316–329.

Mattson, E. C., Nasse, M. J., Rak, M., Gough, K. M. & Hirschmugl, C. J. (2012). *Anal. Chem.* **84**, 6173–6180.

Merk, S., Blume, A. & Riederer, M. (1997). *Planta*, **204**, 44–53.

Mitik-Dineva, N., Wang, J., Truong, V. K., Stoddart, P., Malherbe, F., Crawford, R. J. & Ivanova, E. P. (2009). *Curr. Microbiol.* **58**, 268–273.

Nasse, M. J., Walsh, M. J., Mattson, E. C., Reininger, R., Kajdacsy-Balla, A., Macias, V., Bhargava, R. & Hirschmugl, C. J. (2011). *Nat. Methods*, **8**, 413–416.

Ramananarivo, S., Godoy-Diana, R. & Thiria, B. (2011). *Proc. Natl Acad. Sci.* **108**, 5964–5969.

Sajomsang, W. & Gonil, P. (2010). *Mater. Sci. Eng. C*, **30**, 357–363.

Salta, M., Wharton, J. A., Stoodley, P., Dennington, S. P., Goodes, L. R., Werwinski, S., Mart, U., Wood, R. J. K. & Stokes, K. R. (2010). *Philos. Trans. R. Soc. A*, **368**, 4729–4754.

Stelzer, E. H. K. (1998). *J. Microsc.* **189**, 15–24.

Sun, M., Watson, G. S., Zheng, Y., Watson, J. A. & Liang, A. (2009). *J. Exp. Biol.* **212**, 3148–3155.

Tanaka, H., Matsumoto, K. & Shimoyama, I. (2007). *J. Micromech. Microeng.* **17**, 2485–2490.

Wagner, T., Neinhuis, C. & Barthlott, W. (1996). *Acta Zool.* **77**, 213–225.

Watson, G. S., Cribb, B. W. & Watson, J. A. (2010). *ACS Nano*, **4**, 129–136.

Watson, G. S., Myhra, S., Cribb, B. W. & Watson, J. A. (2008). *Biophys. J.* **94**, 3352–3360.

Webb, H. K., Hasan, J., Truong, V. K., Crawford, R. J. & Ivanova, E. P. (2011). *Curr. Med. Chem.* **18**, 3367–3375.

Xie, G., Zhang, G., Lin, F., Zhang, J., Liu, Z. & Mu, S. (2008). *Nanotechnology*, **19**, 095605.

Yao, X., Song, Y. & Jiang, L. (2011). *Adv. Mater.* **23**, 719–734.

Young, J., Walker, S. M., Bomphrey, R. J., Taylor, G. K. & Thomas, A. L. (2009). *Science*, **325**, 1549–1552.

Zeier, J. & Schreiber, L. (1999). *Planta*, **209**, 537–542.

Zhang, J., Sheng, X. & Jiang, L. (2009). *Langmuir*, **25**, 1371–1376.

Zimmermann, J., Reifler, F. A., Fortunato, G., Gerhardt, L. & Seeger, S. (2008). *Adv. Funct. Mater.* **18**, 3662–3669.